


Research Article

Immuno-PET Imaging of Siglec-15 Using the Zirconium-89-Labeled Therapeutic Antibody, NC318

Elaine M. Jagoda ¹, **Falguni Basuli**², **Colleen Olkowski**¹, **Ido Weiss**³, **Tim E. Phelps**¹, **Karen Wong**¹, **Anita Thien Ton**¹, **Kelly C. Lane**², **Steve Adler**^{1,4}, **Donna Butcher**⁵, **Elijah F. Edmondson**⁵, **Sol Langermann**³ and **Peter L. Choyke**¹

¹Molecular Imaging Branch, National Cancer Institute, Bethesda, MD, USA

²Chemistry and Synthesis Center, National Heart, Lung, and Blood Institute, National Institutes of Health, Bethesda, MD, USA

³NextCure, Beltsville, MD, USA

⁴Clinical Research Directorate, Frederick National Laboratory for Cancer Research, Frederick, MD, USA

⁵Molecular Histopathology Lab, Frederick National Laboratory for Cancer Research, NCI, Frederick, MD, USA

Correspondence should be addressed to Elaine M. Jagoda; ejagoda@mail.nih.gov

Received 10 June 2022; Revised 12 August 2022; Accepted 13 January 2023; Published 9 February 2023

Academic Editor: Henry VanBrocklin

Copyright © 2023 Elaine M. Jagoda et al. This is an open access article distributed under the Creative Commons Attribution License, which permits unrestricted use, distribution, and reproduction in any medium, provided the original work is properly cited.

Objective. Sialic acid-binding immunoglobulin-like lectin 15 (Siglec-15) is overexpressed in various cancers which has led to the development of therapeutic anti-Siglec-15 monoclonal antibodies (mAbs). In these preclinical studies, the therapeutic mAb, NC318 (antihuman/murine Siglec-15 mAb), was labeled with zirconium-89 and evaluated in human Siglec-15 expressing cancer cells and mouse xenografts for potential use as a clinical diagnostic imaging agent. **Methods.** Desferrioxamine-conjugated NC318 was radiolabeled with zirconium-89 to synthesize [⁸⁹Zr]Zr-DFO-NC318. Cancer cell lines expressing variable Siglec-15 levels were used for in vitro cell binding studies and tumor xenograft mouse models for biodistributions. [⁸⁹Zr]Zr-DFO-NC318 biodistribution and PET imaging studies to determine tissue uptakes (tissue:muscle ratios, T:M) included pharmacokinetic evaluation in Siglec-15+tumor xenografts and immunocompetent mice, blocking with nonradioactive NC318 (20, 100, and 300 μg) and xenografts with low/negligible Siglec-15 expressing tumors. **Results.** [⁸⁹Zr]Zr-DFO-NC318 exhibited high affinity ($K_d \sim 4$ nM) for Siglec-15 and distinguished between moderate and negligible Siglec-15 expression levels in cancer cell lines. The highest [⁸⁹Zr]Zr-DFO-NC318 uptakes occurred in the spleen and lymph nodes of the Siglec-15+tumor xenografts at all time points followed by Siglec-15+tumor uptake which was lower although highly retained. In immunocompetent mice, the spleen and lymph nodes exhibited lower uptakes indicating that the athymic xenografts had increased Siglec-15+ immune cells. Specific [⁸⁹Zr]Zr-DFO-NC318 binding to Siglec-15 was proven with NC318 blocking studies in which dose-dependent decreases in Siglec-15+tumor T:Ms were observed. Higher than expected, tumor T:Ms were seen in lower expressing tumors likely due to the contribution of murine Siglec-15+ immune cells in the tumor microenvironment as confirmed by immunohistochemistry. Siglec-15+tumors were identified on PET images whereas low/negligible expressing tumors showed lower uptakes. **Conclusions.** In vitro and in vivo [⁸⁹Zr]Zr-DFO-NC318 uptakes correlated with Siglec-15 expression levels in target tissues. Despite uptake in immune cell subsets in the tumor microenvironment, these results suggest that clinical [⁸⁹Zr]Zr-DFO-NC318 PET imaging may have value in selecting patients for Siglec-15-targeted therapies.

1. Introduction

Sialic acid-binding immunoglobulin-like lectin 15 (Siglec-15) is a cell surface type-1 transmembrane protein that is overexpressed in a variety of tumor types as well as in selected immune cells such as tumor-associated macrophages and dendritic cells. Siglec-15 expression in the tumor microenvironment (TME) is thought to be associated with permissive host immunity conducive to disease progression [1–4]. In addition to modulating tumor immune responses, Siglec-15 is expressed on osteoclasts and plays a role in osteoclast regulation and bone remodeling [5]. These diverse modulatory functions are activated upon Siglec-15 binding to sialoglycan structures such as Neu5Ac α 2-6GalNAc α (sialyl Tn) which is overexpressed in many cancer types including gastric, breast, lung, and ovarian [6]. CD44, a glycoprotein overexpressed on human hepatoma cells, has modified sialoglycans that can also serve as ligands for Siglec-15 thereby promoting tumor cell migration [7, 8]. Hence, Siglec-15 has been identified as an important immunomodulator and potential target for the treatment of osteoporosis and cancer offering certain advantages over other immunotherapeutics. Although Siglec-15 shares structural homology with programmed cell death ligand-1 (PD-L1), the immune regulatory mechanism is distinct and may offer an alternative therapeutic option in cancer patients unresponsive to PD-L1 immunotherapies [9].

In preclinical osteoporosis and tumor mouse models, antibody blockade of Siglec-15 resulted in increasing bone density and tumor regression (by reversing the immunosuppression in the TME), respectively [9–12]. These findings have prompted further development of anti-Siglec-15 monoclonal antibodies (mAbs) for evaluation as immune checkpoint inhibitors in clinical trials which include NextCure's NC318 for solid tumors, Medimmune's mAb for acute myeloid leukemia, and Daichi Sankyo's DS-1501 for osteoporosis [9]. NC318 in a phase I clinical trial which included patients with non-small-cell lung carcinoma (NSCLC), melanoma, ovarian, colorectal, breast, and other types of cancer demonstrated efficacy primarily in patients with NSCLC (20%). This phase I trial was conducted without any biomarker assessment, but the NSCLC patient response rate of 20% was found to correlate with the Siglec-15 positivity of 25.7% (immunohistochemistry, IHC) observed in tumor biopsy stained sections of NSCLC patients (241) from a subsequent study [4, 9]. These results would indicate that tumor Siglec-15 expression may influence the therapeutic response; however, the molecular interactions remain to be elucidated. Hence, a biomarker has yet to be identified that would be predictive of therapeutic responses in patients and aid in patient selection for anti-Siglec-15 mAb therapies.

Radiolabeling of these therapeutic anti-Siglec-15 mAbs for immuno-positron emission tomography (immuno-PET) imaging could prove useful in quantitating *in vivo* expression levels of Siglec-15 in tumors in real time potentially aiding in patient selection, monitoring changes in Siglec-15 over a treatment time course, and determining the relationship of Siglec-15 expression levels to

patient therapeutic responses. Although these therapeutic mAbs possess the high affinity and specificity required for a successful PET imaging agent, long lived PET radionuclides such as zirconium-89 ($t_{1/2} = 78.4$ h) are required to match the long biological half-life of mAbs. In this report, a therapeutic humanized IgG₁ mAb which recognizes both human and murine Siglec-15, NC318, was labeled with zirconium-89 for preclinical evaluation of Siglec-15 targeting and potential to serve as a biomarker for patient selection and therapeutic responses. These preclinical studies included both *in vitro* binding assays with human melanoma and NSCLC cancer cells with varying Siglec-15 expression levels and *in vivo* biodistribution studies in tumor-bearing mouse xenograft models using the same cell lines to determine the clinical potential of [⁸⁹Zr]Zr-DFO-NC318.

2. Materials and Methods

Humanized IgG₁ monoclonal Ab, anti-Siglec-15 mAb (NC318), was kindly provided by Dr. Ido Weiss (NextCure, Beltsville, MD, USA). The p-isothiocyanatobenzyl-desferrioxamine (DFO-Bz-NCS) was purchased from Macrocytics, Inc. (Plano, TX, USA). Sodium acetate and Tris-HCl were purchased from Thermo Fisher Scientific (Waltham, MA, USA). The lyophilized whole human serum was obtained from MP Biomedicals, LLC (Solon, OH, USA) and dissolved in 2 mL saline. This serum solution was directly used without inactivation for the stability study of [⁸⁹Zr]Zr-DFO-NC318. All other chemicals and reagents were purchased from Sigma-Aldrich (St. Louis, MO, USA) and used without further purification. PD-10 desalting columns were obtained from GE Healthcare Biosciences (Pittsburgh, PA, USA). Zirconium-89 oxalate was obtained from 3D Imaging (Little Rock, Arkansas, USA). Analytical high-performance liquid chromatography (HPLC) analyses were performed on an Agilent 1200 Series instrument equipped with a multiwavelength UV detector connected in series with a Bioscan flow count radiodetector. HPLC was performed using a size exclusion column (SE, 4.6 : mm ID \times 30 cm, 4 μ m), TSKgel SuperSW3000, obtained from Tosoh Bioscience LLC (King of Prussia, PA, USA) and an eluent system comprised of 0.1 M sodium phosphate (pH 6.8), 0.1 M sodium sulfate, 0.05% sodium azide, and 10% isopropyl alcohol at a flow rate of 0.3 mL/min. The gel filtration standard (cat #151-1901) for calibration of the size exclusion column was obtained from Bio-Rad (Hercules, California, USA). The iTLC papers, TEC-control-chromatography strips, model#150-771, were obtained from Biodex Medical Systems, Inc. (Shirley, New York, USA). The iTLC papers were developed using 0.1 M EDTA (pH 7) and read in an Eckert & Ziegler TLC scanner (B-AR2000-1, Hopkinton, MA, USA). A bicinchoninic (BCA) Protein Assay Kit (Thermo Fisher Scientific) with bovine gamma globulin standard was used to determine the conjugate concentrations.

2.1. Synthesis of the DFO-NC318 Conjugate and Zirconium-89-Labeled NC318 ([⁸⁹Zr]Zr-DFO-NC318). The DFO-NC318 conjugate was prepared following the literature

method using a 5-fold molar excess of DFO-Bz-NCS [13]. The purity of DFO-NC318 was determined by HPLC using a size exclusion column (SE-HPLC). The concentration (5.7 mg/mL) of the conjugates was measured using the BCA assay. The chelator to antibody ratio was 1.3, as determined by Liquid Chromatography Electro Spray Ionization Mass Spectrometry (LC-ESI-MS) using an Acquity UPLC H-Class coupled to a Xevo G2-XS QToF (Waters Corporation). The sample was deglycosylated using Rapid PNGase F (New England BioLabs) prior to analysis and desalted online using an XBridge Protein BEH C4 column (Waters Corporation) with a water/acetonitrile gradient containing 0.1% formic acid. Data processing was performed using UNIFI software (Waters Corporation), and peaks were assigned based on the unmodified antibody as a reference. Zirconium-89 conjugate (^{89}Zr]Zr-DFO-NC318) was prepared according to the literature method with minor modifications [13].

Briefly, a stock solution of zirconium-89 oxalate (~440 MBq) was diluted with 300 μL of HEPES buffer (0.5 M, pH 7.1-7.3). From this stock solution, ~150 MBq of zirconium-89 was used per radiolabeling reaction. The aliquot of zirconium-89 (~150 MBq, 110 μL) was further diluted with HEPES buffer (0.5 M, 800 μL , pH 7.1-7.3). 2,5-Dihydroxybenzoic acid (20 μL , ~5 mg/mL in water, pH adjusted to 7 with 2 M Na_2CO_3 solution) was added followed by a solution of DFO-NC318 (0.4 mg, 5.7 mg/mL, 70 μL). The reaction mixture was incubated for 1 h at room temperature and challenged with DTPA (5 μL , 0.1 M, pH 7) for an additional 10 min. The radiolabeled conjugate was purified by PD-10 column using 0.9% NaCl (pH 7). The molar activity and the purity of the radiolabeled conjugate were determined by SE-HPLC ($t_R = 7.4$ min). The identity of the ^{89}Zr]Zr-DFO-NC318 was confirmed by comparing the retention time (based on UV 280) with DFO-NC318 ($t_R = 7.4$ min) and the gel filtration standard.

2.2. Storage and In Vitro Serum Stability. Following radio-synthesis, a saline solution of ^{89}Zr]Zr-DFO-NC318 was stored at 4°C for 48 h and analyzed every 24 h by SE-HPLC to determine storage stability (Supplementary Information Figure S1 and Table S1). To determine serum stability, whole human serum (500 μL) was added to a solution of ^{89}Zr]Zr-DFO-NC318 (~500 μCi in 500 μL of saline, pH 7.0) and kept at 37°C for up to 7 d. The radiochemical stability was determined every 24 h by directly injecting an aliquot of the solution into the HPLC and by iTLC (Supplementary Information Figure S2, Figure S3, and Table S2).

2.3. Cell Lines. Cell lines were grown at 37°C in 5% CO_2 in DMEM (624-MEL WT/624-MEL+S15 human melanoma wild type or transduced with Siglec-15, provided by Dr. Ido Weiss (NextCure, Beltsville, MD, USA)), RPMI-1640 (LOX-IMVI (human melanoma); ATCC), and RPMI-1640 ATCC modified with 10 mM HEPES and 4500 mg/L glucose (HCC-827 (human non-small-cell lung carcinoma); ATCC). All media were supplemented with 10% FBS, 2 mM L-glutamine, and Pen/Strep.

2.4. In Vitro Studies. Saturation binding studies were performed to determine the K_d and B_{max} with 624-MEL WT/+S15 and LOX-IMVI cells in plates ($2-10 \times 10^5$ cells/well) or tubes ($2-10 \times 10^5$ cells/tube) to which increasing concentrations of ^{89}Zr]Zr-DFO-NC318 (0.25-25 nM) were added to duplicate wells or tubes; nonspecific binding was determined by adding nonradioactive NC318 mAb (10^{-6} M) to another set of duplicates. For competition studies, increasing concentrations (0-1000 nM) of nonradioactive NC318 were added to a constant concentration of ^{89}Zr]Zr-DFO-NC318 (0.75 to 2.0 nM) and 624-MEL+S15 cells. After incubation (2 h, 4°C), the cell bound ^{89}Zr]Zr-DFO-NC318 was separated from the free radiolabeled antibody either: (1) plated cells were washed with phosphate-buffered saline (PBS), treated with trypsin, and collected in vials; or (2) cells in tubes were pelleted by centrifugation, washed twice (PBS), and supernatants removed. The cell bound radioactivity for these samples was determined by gamma counting (Perkin Elmer 2480 Wizard3, Shelton, CT). From the saturation studies, the K_d and B_{max} were determined from 6 to 8 concentrations of ^{89}Zr]Zr-DFO-NC318 and analyzed using nonlinear regression curve fitting (one-site specific binding); from the competition studies, K_i 's were determined from 8 to 10 competitor concentrations (Prism (version 5.04 Windows), GraphPad software, San Diego, CA).

The biological specific activity or immunoreactive fraction (% immunoreactivity) of the ^{89}Zr]Zr-DFO-NC318 was determined by a self-displacement method described by Choi et al. and Morris in which the % immunoreactivity was derived from a ^{89}Zr]Zr-DFO-NC318 saturation curve and competition curve using as the competitor, nonradioactive NC318 (described above) [14, 15].

2.5. Mouse Models. Female athymic nude mice (Ncr-nu/nu, NCI-Frederick, MD) were injected subcutaneously in the right shoulder with 624-MEL WT/+S15 cells (2×10^6 [6]), LOX-IMIV cells ($2-4 \times 10^6$ [6]), and HCC-827 cells ($1-2 \times 10^6$ [6]) in PBS:30% Matrigel. Female Balb/c mice (BALB/c AnNCr, Charles River Laboratories, Wilmington, MA) were used as the immunocompetent mouse model. Animal studies were performed in accordance with Institutional Guidelines for the Care and Use of Laboratory Animals using IACUC approved protocols.

2.6. Biodistribution Studies. Tumor-bearing mice (tumor weights: 0.1-0.8 g) were injected intravenously (tail vein) with ^{89}Zr]Zr-DFO-NC318 (0.37-0.74 MBq (10 to 30 μCi , 2 to 10 pmol)) and euthanized (via CO_2 inhalation) at selected times. Blood samples and tissues were excised from each animal and weighed, and radioactivity content was determined (PerkinElmer 2480 Wizard3). For the NC318 blocking studies, mice were injected with ^{89}Zr]Zr-DFO-NC318 only or coinjected with nonradioactive NC318 (20 μg (24x; 133 pmol), 100 μg (113x; 667 pmol), and 300 μg (309x; 2001 pmol). Blood and tissues were excised from each animal and weighed, and radioactivity content was determined (PerkinElmer 2480 Wizard3). Radioactivity content in the blood and each tissue was expressed as % injected dose per gram of tissue (%ID/g; (1)) and then

normalized for body weight to a 20 g mouse (2) from which tissue : muscle ratios (T : M; (3)) were determined as follows:

- (1) $\%ID/g = ((\text{counts per minute (cpm)})_{\text{tissue}} / \text{tissue weight (g)}) / \text{cpm}_{\text{total injected dose}} \times 100$
- (2) $\%ID/g_{(\text{normalized to a 20 g mouse})} = (\%ID/g) \times (\text{body weight} / 20 \text{ g})$
- (3) $T : M = \%ID/g_{\text{tissue}} / \%ID/g_{\text{muscle}}$

Statistical analysis of the differences between the 2 groups was assessed using the Student *t*-test with $P < 0.05$ as significant (GraphPad InStat 3 for Windows).

2.7. PET/CT Imaging Studies. Tumor-bearing mice were anesthetized with isoflurane/O₂ (1.5%-3% *v/v*) and imaged at various times after intravenous injection of [⁸⁹Zr]Zr-DFO-NC318 (2.6 to 5.55.7 MBq (70 to 150 μ Ci), 15 to 50 pmol). Whole body static PET images were obtained at 2 bed positions (FOV = 2.0 cm and total imaging time : 10 min) followed by CT images (2 bed positions, 10 min) using the BioPET scanner (Bioscan Inc., Washington, DC, USA). The images were reconstructed with a 3-dimensional ordered-subset expectation maximum (3D-OSEM).

2.8. Human Siglec-15 Dosimetry Estimation. Human dosimetry estimates extrapolated from the mouse biodistribution studies were calculated using OLINDA V1.1 (Vanderbilt University, TN) with the mouse to human fractional organ extrapolation of the mean residence times of the ligand measured by the biodistribution described above. The %ID/g values (determined from the biodistribution studies described above) for a set of organs determined over a 7 d time course were used to extrapolate human dosimetry in the same organs. The whole organ was dissected from the carcass and counted to measure the organ's radioactive content. For the bone, skin, muscles, and blood samples, a sample was dissected, weighed, and counted in the gamma counter. Because of the relatively small uptake in the skin, muscle, and blood, these tissues were not included in the kinetic input form of the OLINDA dosimetry estimation software.

Biodistribution data showed radioconjugate uptake in the mouse skeleton above the background. To account for this, a special case was made for bone dosimetry estimation. Instead of including the bone activity in the body remainder volume, the whole bone activity was estimated and entered into the trabecula bone input field in OLINDA. The bone tissue %ID/g and the %ID/organ were estimated using a murine bone fraction model of 53.3 (g/kg) [16]. This calculation gives an estimated bone mass of 1.07 g for a 20 g mouse. The %ID/g at each time point for each mouse was multiplied by the bone mass fractional estimate for each mouse.

From the %ID/organ, time activity curves (TAC) were generated from PET images and residence times were calculated in units of hours. Between the time points of the TAC, a trapezoidal model was used to estimate the area under the curve. For the last time point, an exponential decay curve

with the half-life of zirconium-89 was used to extrapolate the tail of the TAC. Since the %ID/organ of the whole intestine was measured (including the contents), the absorbed activity between the large and small intestines was estimated by the MOBY fractional mass model for a 25 g mouse [17]. The result was that 75% of the activity was assigned to the small intestine and 25% to the large intestine. The large intestine was further separated using the ICRP 80 standard in which 57% of the radioactivity was assigned to the upper and the remaining 43% assigned to the lower large intestine.

2.9. Histopathology and Immunohistochemistry. All tissues were fixed in 10% neutral buffered formalin, routinely processed and sectioned at 5 μ m for automated H&E staining, and digitized with an Aperio ScanScope XT (Leica) at 200x in a single *z*-plane. Slides and digital images were reviewed by a board-certified veterinary pathologist. Immunohistochemistry (IHC) staining was performed for Siglec-15 (1F7, rabbit monoclonal, HIER with decloak citrate, 1:15,000, overnight at 72°F), CD45(BD Biosciences 550539, rat monoclonal, HIER citrate, 1:100, overnight at 72°F), CD31 (Abcam ab28364, HIER EDTA, 1:100, 60 min) [18], Iba1 (Biocare CP290, rabbit polyclonal, HIER citrate, 1:500, 20 min), and NUMA-1 (Lifespan LS-B11047, rabbit polyclonal, HIER citrate, 1:75, 20 min). All staining was performed on Leica Biosystems BondMax autostainer or incubated overnight at room temperature. Positive controls included mouse spleen (CD45 and Iba1) and human 624-MEL+S15 xenografts (Siglec-15 and NUMA-1). Biological negative controls included human 624-MELWT tumors (Siglec-15 and NUMA-1); technical negative controls included replacing the primary antibody with a nonspecific antibody from the same species and of the same isotope. The IHC reaction was visualized with DAB, followed by hematoxylin counterstain.

Whole slide imaging (WSI) was performed with an Aperio ScanScope XT (Leica) at 200x in a single *z*-plane. Digital pathology for biomarker quantification was performed following WSI with thresholds for positivity determined using known positive controls. Tumor necrosis was estimated using random forest machine learning algorithms on H&E images. Microvessel density was estimated using CD31 stained tissue sections with an object detection algorithm. CD45 and Iba1 positive cells are reported as number of positive cells per mm². Cell detection algorithms were run to quantify positive cells, which are expressed as the number of positive cells per mm² of tissue and the percent of CD45 and Iba1 positive cells. Siglec-15 expression is reported as an *H*-score in which the proportion of all cells (tumor, spleen, or lymph node) found to express Siglec-15 was determined and then multiplied by the staining intensity score to obtain a final semiquantitative *H*-score (maximum value of 300 corresponding to 100% of cells positive for Siglec-15 with an overall staining intensity score of 3). Dual immunofluorescence for NUMA1 (human marker) and Siglec-15 was performed as Siglec-15 is reactive with both mouse and human. Immunofluorescence staining of human tumor cells was differentiated from mouse cells based on a positive NUMA1 nuclear signal.

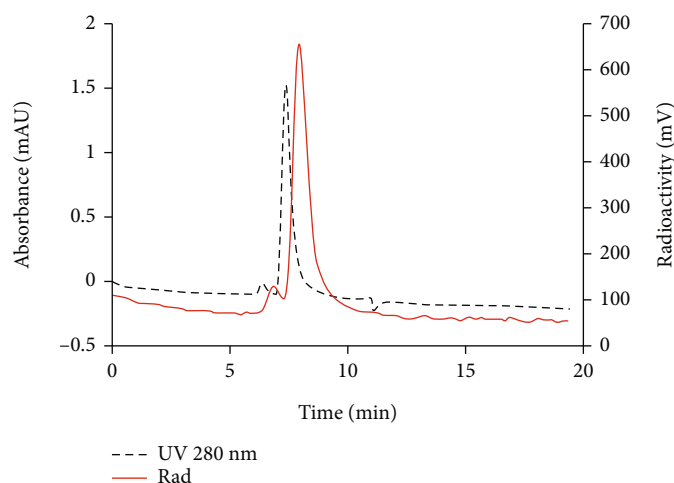


FIGURE 1: A representative HPLC of [^{89}Zr]Zr-DFO-NC318. HPLC condition: eluent, 0.1 M sodium phosphate, 0.1 M sodium sulfate, 0.05% sodium azide, 10% isopropyl alcohol (pH 6.8), and flow rate 0.3 mL/min.

3. Results

3.1. Radiochemistry. Zirconium-89-labeled DFO-NC318 conjugate was prepared following the literature method with minor modifications [13]. The isolated radiochemical yields were in the range of 85-95% ($n = 20$) with radiochemical purity > 95% (Figure 1). The molar activities of the radioimmunoconjugates were 22,200-70,300 MBq/ μmol ($n = 15$). To determine the storage stability, a saline solution of [^{89}Zr]Zr-DFO-NC318 was kept at 4°C and monitored by SE-HPLC every 24 h. A slow decomposition was observed (91% intact after 48 h; Supporting information Figure S1 and Table S1). Whole human serum stability determined by SE-HPLC at 37°C indicated 48% decomposition in 4 days (Supporting information Figure S2 and Table S2) and remained unchanged from 4 d to 7 d. As free zirconium-89 is often trapped on a SE-column to a significant degree, iTLC analysis was performed on days 3-7 to assess the presence of free zirconium-89. The iTLC results indicated the formation of ~15% free zirconium-89 in 4 d which remained relatively constant until 7 d. The amount of intact [^{89}Zr]Zr-DFO-NC318 based on iTLC after 7 d was ~60%, similar to the SE-HPLC results (Supporting information Figure S3).

3.2. In Vitro Cell Binding Studies. High specific binding and affinity ($K_d = 4.01 \pm 0.474$ nM ($n = 6$)) was displayed by [^{89}Zr]Zr-DFO-NC318 for Siglec-15 in saturation binding studies with 624-MEL+S15 cells (high/moderate Siglec-15 expression; Figure 2(a)). The 624-MEL+S15 cells exhibited the highest Siglec-15 expression levels ($B_{\text{max}} = 148,465 \pm 18,676$ sites per cell ($n = 6$)) which were significantly increased compared to LOX IMIV cells ($B_{\text{max}} = 26,970 \pm 3,863$ sites per cell ($n = 4$); $P = 0.0009$), HCC-827 cells ($12,831 \pm 2,264$ sites per cell ($K_d = \text{constant}$; $n = 3$); $P = 0.0016$), and 624-MEL WT cells ($B_{\text{max}} = 13,298 \pm 2,759$ sites per cell ($K_d = \text{constant}$; $n = 3$); $P = 0.017$; Figure 2(b)). The moderately lower Siglec-15 expression levels of the LOX IMIV cells were significantly higher than the 624-MEL WT cells ($P = 0.0443$) and HCC-827 cells

($P = 0.0355$) whereas the lower Siglec-15 expression levels of the 624-MEL WT cells and HCC-827 cells were comparable. Nonspecific binding (B_{ns}) comprised the greater part of the binding with the 624-MEL WT and HCC-827 cells ranging from 57% to 96%. The moderate and low Siglec-15 expression levels of LOX IMIV and HCC-827, respectively, found in these binding studies were consistent with published results using flow cytometry [4, 19]. These in vitro results indicate that [^{89}Zr]Zr-DFO-NC318 distinguishes between minimal to moderate Siglec-15 expression levels and would be appropriate for in vivo imaging of tumors with high to moderate Siglec-15 expression levels as was observed with the 624-MEL+S15 cells and potentially LOX IMIV. Conversely, tumors with lower Siglec-15 expression levels (<27,000 sites per cell) as in the case of 624-MEL WT and HCC-827 cells may not be clearly discernable from the background.

From [^{89}Zr]Zr-DFO-NC318 competition studies, the K_i of the nonradioactive NC318 was determined as 3.73 ± 0.341 nM ($n = 6$) which was comparable to the K_d (4.01 ± 0.474 nM) of [^{89}Zr]Zr-DFO-NC318. These results demonstrated that the high affinity binding of the mAb to Siglec-15 was retained after conjugation of NC318 with DFO followed by radiolabeling with zirconium-89 (Figure 3(a)). The Morris self-displacement method to determine the biologically active fraction or immunoreactive fraction (% immunoreactivity) of [^{89}Zr]Zr-DFO-NC318 ($90.0 \pm 3.0\%$; $n = 6$ batches) indicated the preservation of the biological activity and reproducibility across batches (Figure 3(b)).

3.3. In Vivo Biodistribution Studies. In normal immunocompetent mice (Balb/c) and 624-MEL+S15 xenograft nude mice, [^{89}Zr]Zr-DFO-NC318 biodistributions were determined at 1, 2, 3, and 6 or 7 d post injection (Figures 4(a) and 4(b)). In the Balb/c and 624-MEL+S15 xenograft mice, [^{89}Zr]Zr-DFO-NC318 distribution was rapid with clearance from the blood and most nontarget tissues with the exceptions of the liver, kidney, and femur which most likely were not decreasing over the time course due to the contribution

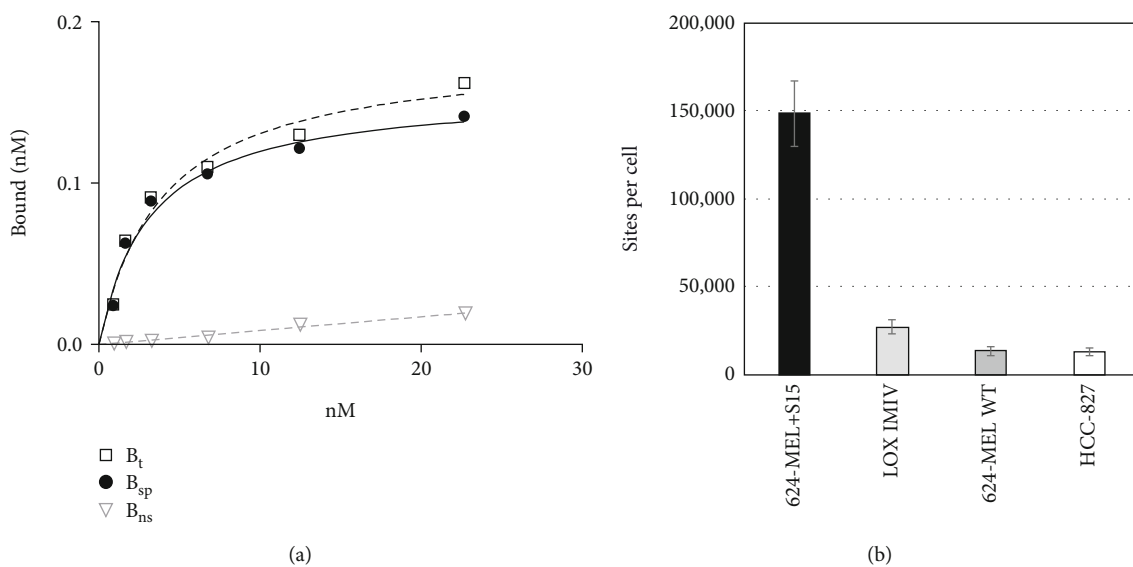


FIGURE 2: (a) Representative plot from an in vitro ^{89}Zr -DFO-NC318 saturation binding assay using 624-MEL+S15 cells with each point representing the average of duplicates; for this plot: $K_d = 3.14 \pm 0.74$ nM, $B_{\max} = 0.157 \pm 0.012$ nM (1.89×10^5 sites/cell); $B_{\text{nonspecific}}$ (B_{ns}) determined in the presence of 10^{-6} M NC318; B_{specific} (B_{sp}) = B_{total} (B_t) - B_{ns} . (b) Siglec-15 concentrations (B_{\max} , sites per cell) in 624-MEL+S15, LOX IMIV, HCC-827, and 624-MEL WT cancer cell lines determined from in vitro saturation binding assays; each bar represents the mean \pm SE ($n = 6$ (624-MEL+S15), $n = 4$ (LOX IMIV), and $n = 3$ (624-MEL WT and HCC-827)).

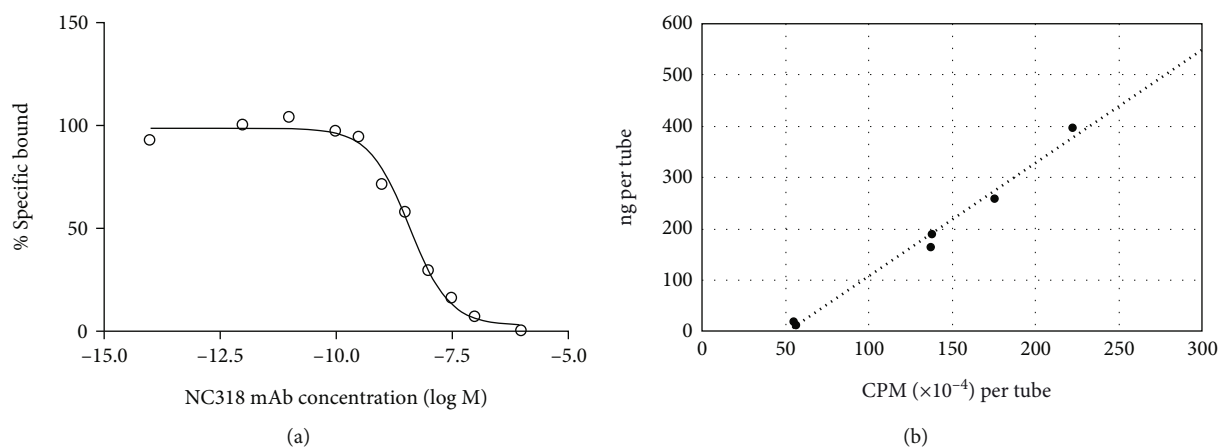
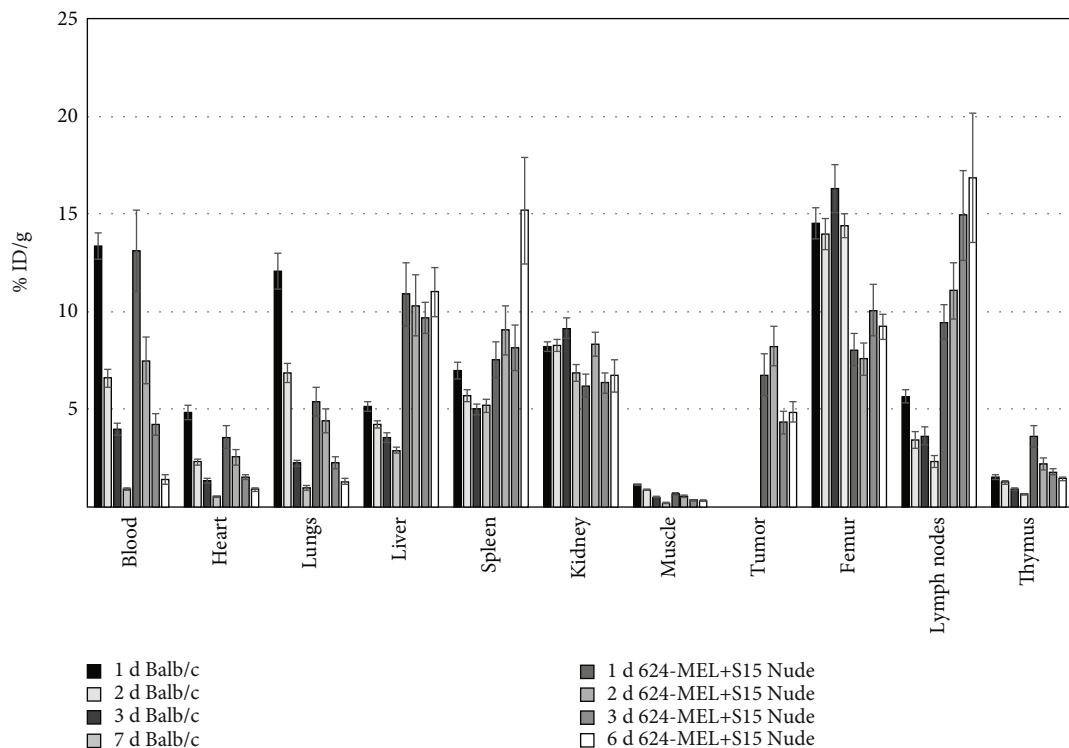


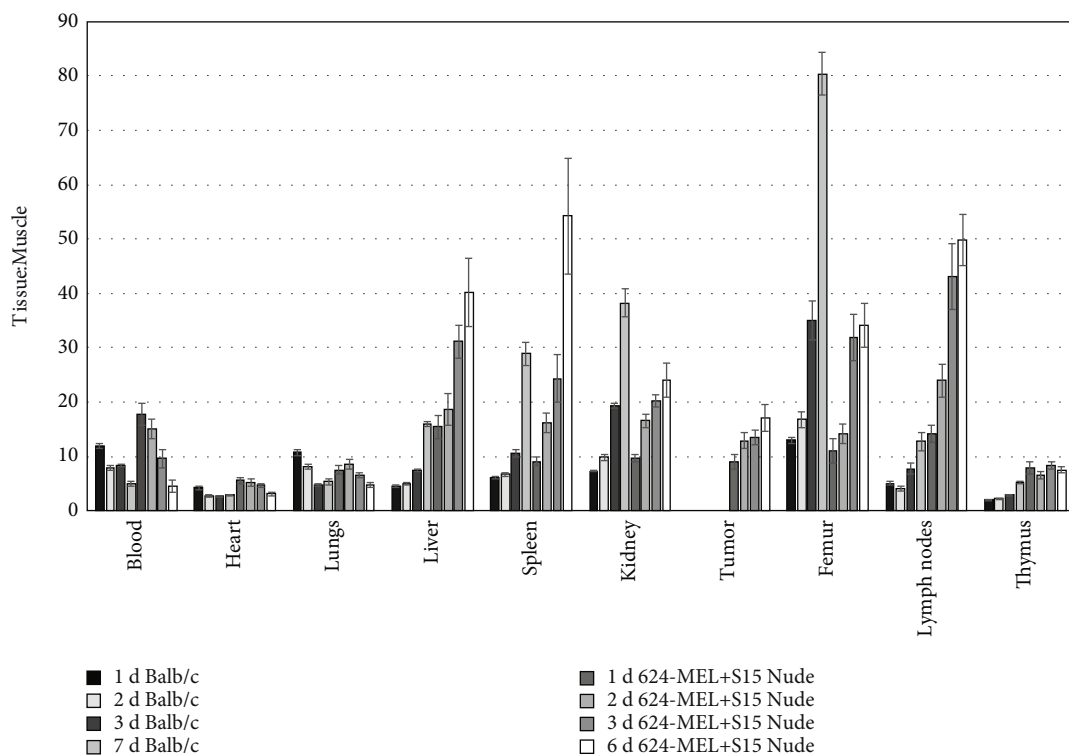
FIGURE 3: (a) Representative plot from an in vitro ^{89}Zr -DFO-NC318 competition-binding assay using NC318 (self-displacement (Morris method)) with 624-MEL+S15 cells. Each point (average of duplicates) represents % specific bound ($K_i = 2.44 \pm 0.44$ nM). (b) Representative plot for the determination of the immunoreactivity fraction (% immunoreactivity) of ^{89}Zr -DFO-NC318 (same batch) using the Morris method (for this plot: linear regression curve fit, $y = 2.21x - 114.34$, $R^2 = 0.99$; % immunoreactivity = 84%).

of radioactive metabolites and released zirconium-89 (Figure 4(a)). Although clearance from the blood was comparable for the Balb/c and 624-MEL+S15 xenograft mice, other differences were observed in the targeting and pharmacokinetics of ^{89}Zr -DFO-NC318. The highest tissue uptakes (%ID/g) were observed in the femur (14.0-16.3%ID/g), kidney (6.8-9.1%ID/g), and spleen (5.0-7.0%ID/g) in the Balb/c mice whereas in the 624-MEL+S15 xenograft mice, the highest uptakes were observed in the lymph nodes (9.4-16.9%ID/g), liver (9.7-11.0%ID/g), and spleen (7.5-11.0%ID/g). The high uptakes in the lymph nodes and spleen as well as the retention of ^{89}Zr -DFO-

NC318 over the time course would be consistent with targeted binding since these tissues are known to have Siglec-15+ cell populations (macrophages). However, in the case of the liver and the femur, only part of the radioactive uptake may represent specific Siglec-15-targeted uptake by hepatic macrophages and bone myeloid cells (osteoclasts), respectively. Previous findings have demonstrated that zirconium-89 released from the DFO chelate tends to be deposited in the epiphysis of the bone [20]. The tumors of the 624-MEL+S15 xenograft mice exhibited stable ^{89}Zr -DFO-NC318 uptakes from 1 d (6.7%ID/g) to 7 d (4.9%ID/g) with a statistically insignificant loss of 28%. This



(a)



(b)

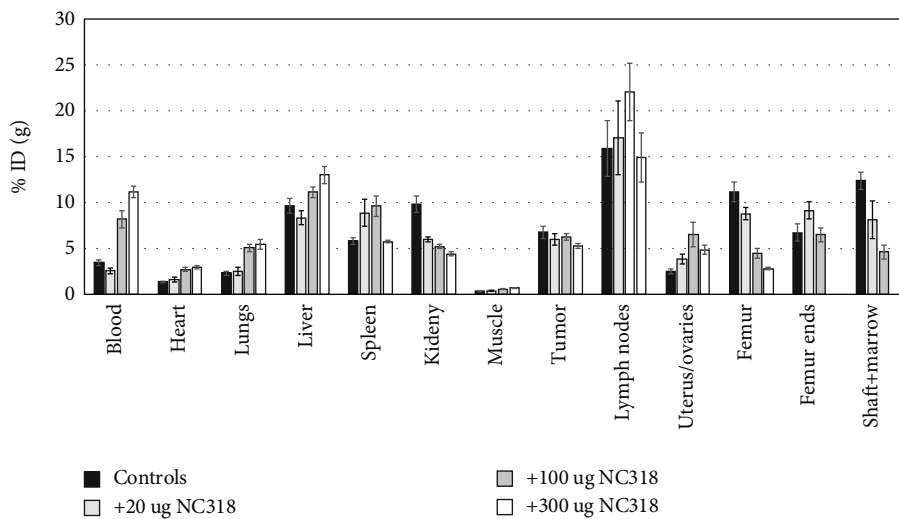
FIGURE 4: (a) Biodistribution (%ID/g (normalized to 20 g mouse)) of $[^{89}\text{Zr}]\text{Zr-DFO-NC318}$ in MEL-624+S15 nude xenograft and Balb/c mice (immunocompetent) from 1 d to 7 d. Each bar represents the mean %ID/g \pm SE of $[^{89}\text{Zr}]\text{Zr-DFO-NC318}$ ($n = 7$ to 10 for each time point). (b) Tissue (%ID/g) to muscle (%ID/g) ratios of $[^{89}\text{Zr}]\text{Zr-DFO-NC318}$ in MEL-624+S15 nude xenograft and Balb/c mice from 1 d to 7 d. Each bar in the graph represents the mean ratio \pm SE of $[^{89}\text{Zr}]\text{Zr-DFO-NC318}$ ($n = 5$ or 6 each time point).

lower 624-MEL+S15 tumor uptake indicates lower levels of Siglec-15 compared to the spleen and lymph nodes which is in concordance with the modest expression levels found in vitro for this cell line. In the immunocompetent Balb/c mice, the highest tissue to muscle ratios (T:M) occurred at 3 d and 7 d in the femur (35:1 T:M (3 d) and 80:1 T:M (7 d)), kidney (19:1 T:M (3 d) and 38:1 T:M (7 d)), and spleen (11:1 T:M (3 d) and 29:1 T:M (7 d)) which progressively increased over the time course (Figure 4(b)). This differed from the 624-MEL+S15 xenograft mice in which peak T:Ms were observed at 3 d and 7 d in the lymph nodes (43:1 T:M (3 d) and 50:1 T:M (7 d)) and liver (31:1 T:M (3 d) and 40:1 T:M (7 d)). In addition, high T:Ms for the 624-MEL+S15 xenograft mice were observed in the spleen (24:1 T:M (3 d) and 54:1 T:M (7 d)) and femur (32:1 T:M (3 d) and 34:1 T:M (7 d)) at the later times. The high T:Ms in the spleen and lymph nodes with the subsequent increases over the time course most likely occurred due to a faster clearance from the muscle, a nontarget tissue, compared to a target tissue in which [⁸⁹Zr]Zr-DFO-NC318 is retained as a result of specific Siglec-15 binding. However, in the case of the T:M increases in the liver and femur at later times, the total radioactive content may only in part represent specific Siglec-15 uptake but radioactive metabolites (including released zirconium-89) which would be expected to increase at later time points as well. Similarly, the tumor T:Ms steadily increased over time from 9:1 to 17:1 indicating Siglec-15 targeting but lower expression levels compared to the lymph nodes and spleen of the 624-MEL+S15 xenograft mice. Over the time course, the Balb/c mice had lower blood and liver T:Ms with higher kidney and femur T:Ms at 7 d compared to the 624-MEL+S15 xenografts indicating that the Balb/c mice had faster clearance and metabolism of [⁸⁹Zr]Zr-DFO-NC318. The Balb/c mice were 8 weeks younger than the 624-MEL+S15 mice which may in part account for the faster pharmacokinetics in nontarget tissues, but the other differences in the T:M values of the blood and Siglec-15+ tissues may be representative of compensatory alterations in immune cell populations in the athymic 624-MEL+S15 xenograft mice. In the 624-MEL+S15 xenograft mice, the lymph node T:Ms were significantly increased 3- to 6-fold ($P < 0.0015$; all time points) compared to the Balb/c mice at all times. T:Ms in the thymus and spleen were also significantly increased, but less, ranging between 1.4- to 4-fold ($P < 0.017$; all time points) and 1.4- to 2.4-fold ($P < 0.05$; all time points except 6 d), respectively. These results suggest that tumor-bearing athymic mice may have increased Siglec-15+ immune cells compared to the Balb/c mice with a full complement of immune cells.

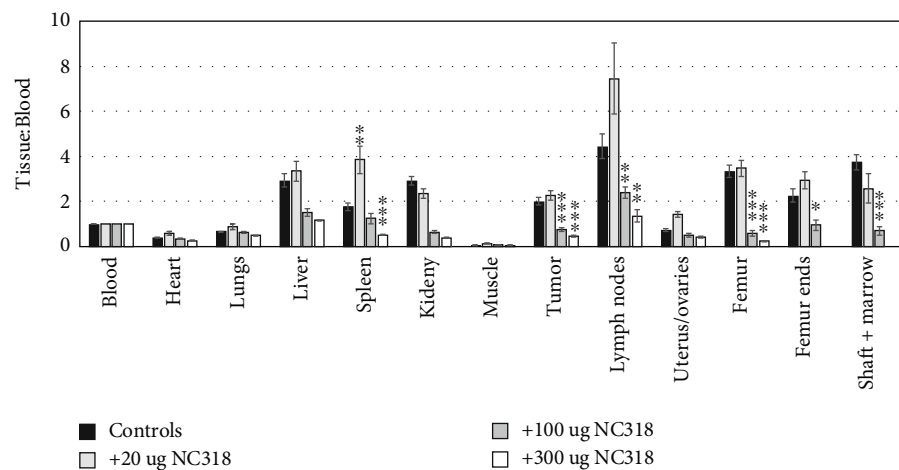
Other blocking biodistributions with unlabeled NC318 were carried out after 3 d of uptake using 624-MEL+S15 xenograft mouse groups injected with [⁸⁹Zr]Zr-DFO-NC318 or coinjected with [⁸⁹Zr]Zr-DFO-NC318 + unlabeled NC318 (20, 100, and 300 μ g) (Figures 5(a)–5(c)). With the lowest NC318 dose of 20 μ g (24x), blood and tissue uptakes (%ID/g) were comparable to the [⁸⁹Zr]Zr-DFO-NC318 control group (~0.8 μ g associated mass) except for a significant increase of 1.5-fold in the uterus/ovaries (3.85%ID/g; $P =$

0.0118) and a significant decrease of 39% in the kidneys (5.97%ID/g; $P = 0.0004$) vs. the uterus/ovaries (2.15%ID/g) and kidneys (9.85%ID/g) in controls, respectively (Figure 5(a)). The radioactive blood content significantly increased 2.4-fold in the NC318 100 μ g dosed group (8.18%ID/g; $P = 0.0001$) and 3.2-fold in the NC318 300 μ g group (11.17%ID/g; $P < 0.0001$) compared to the blood of the control group (3.46%ID/g). This increase of [⁸⁹Zr]Zr-DFO-NC318 in blood with higher mAb blocking doses (> 100 μ g) has been observed with other zirconium-89-labeled mAbs which has been postulated to result from the unlabeled mAb blocking specific uptake in other tissue target sites (i.e., lymph nodes and femur) thereby leaving a greater concentration of radiolabeled mAb in the blood [13, 21]. Since this has affected the [⁸⁹Zr]Zr-DFO-NC318 input function, tissue:blood (T:B) and tissue:muscle (T:M) ratios were determined to provide more accurate quantitative measures of Siglec-15 targeting and changes in specific uptake caused by the NC318 blockade (Figures 5(b) and 5(c)). At the 20 μ g NC318 dose, the tissue:blood ratios (T:B) of the spleen (3.86 T:B) and uterus/ovaries (1.42 T:B) were the only Siglec-15+ tissues which were significantly increased by ~2-fold compared to the control spleen (1.77 T:B) and uterus/ovaries (0.74 T:B) T:Bs. Lymph nodes, spleen, tumor, and femur T:Bs decreased as higher doses of NC 318 > 20 μ g were employed indicating a dose-dependent displacement of [⁸⁹Zr]Zr-DFO-NC318 from these Siglec-15+ tissues. At the NC318 doses of 100 μ g and 300 μ g, T:Bs were significantly decreased in lymph nodes by 46% and 69% ($P < 0.006$), femur by 82% and 92% ($P < 0.0001$), and tumors by 63% and 76% ($P < 0.0001$), respectively, compared to corresponding control T:Bs (Figure 5(b)). In contrast, spleen T:Bs only significantly decreased at the 300 μ g NC318 dose compared to the control group (71%; $P < 0.0001$; Figure 5(b)). In a similar manner, the tissue:muscle ratios (T:Ms) of the lymph nodes, spleen, tumor, and femur were decreased with increasing NC318 doses compared to corresponding T:Ms of the control (Figure 5(c)). For the most part, the blocking of [⁸⁹Zr]Zr-DFO-NC318 uptake with NC318 in target tissues such as lymph nodes, spleen, and in part the femur (bone marrow) would indicate specific [⁸⁹Zr]Zr-DFO-NC318 binding to Siglec-15+ cell populations.

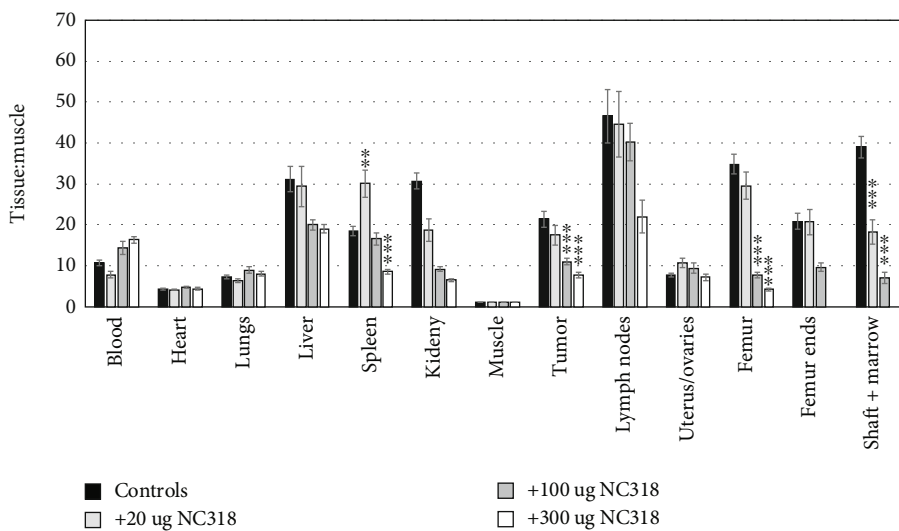
Biodistribution studies after 3 d of uptake were performed with other tumor xenograft models using tumor cell lines with moderate (624-MEL+S15 and LOX IMIV) and low/negligible (624-MEL WT and HCC-827) Siglec-15 expression levels to assess the ability of [⁸⁹Zr]Zr-DFO-NC318 to distinguish quantitative changes in Siglec-15 levels in vivo (Figures 5(d) and 5(e)). The highest [⁸⁹Zr]Zr-DFO-NC318 uptake was observed in the 624-MEL+S15 tumor (6.75%ID/g) which was not significantly different from the LOX IMIV tumor uptake (5.20%ID/g). In contrast, the HCC-827 (4.49%ID/g; $P = 0.0379$) and 624-MEL WT (2.87%ID/g; $P < 0.0001$) tumor uptakes were significantly decreased by 34% and 58%, respectively, compared to 624-MEL+S15 tumor uptake (Figure 5(d)). Similarly, the 624-MEL+S15 (21.3 T:M) and LOX IMIV (19.2 T:M) tumor types had the highest T:M ratios which were significantly increased compared to the TMs of the HCC-827 (9.06



(a)



(b)



(c)

FIGURE 5: Continued.

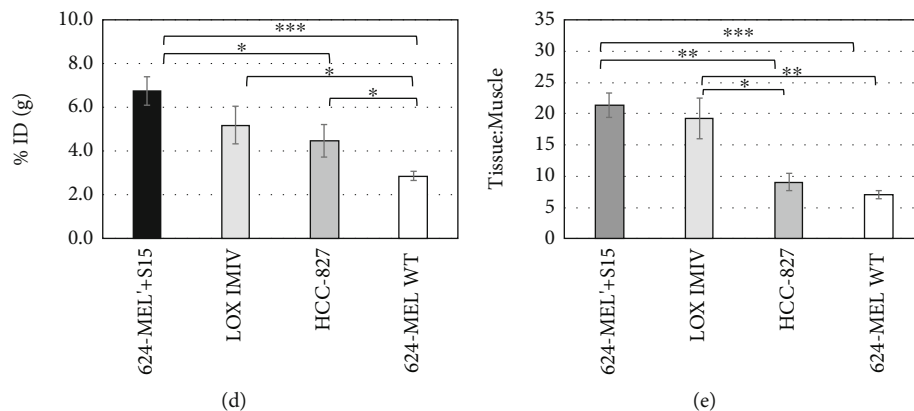


FIGURE 5: (a) Biodistribution (%ID/g) of $[^{89}\text{Zr}]Zr\text{-DFO-NC318}$ in 624-MEL+S15 xenografts at 3 d after receiving coinjections of $[^{89}\text{Zr}]Zr\text{-DFO-NC318}$ ($\sim 0.8 \mu\text{g}$) + NC318 (0 (control), 20, 100, and 300 μg). Each bar represents the mean %ID/g \pm SE ($n = 5\text{-}10$ for each group). (b, c) $[^{89}\text{Zr}]Zr\text{-DFO-NC318}$ tissue (%ID/g) to blood (%ID/g) ratios (T:B; (b)) or tissue (%ID/g) to muscle (%ID/g) ratios (T:M; (c)) in 624-MEL+S15 xenografts 3 d after receiving coinjections of $[^{89}\text{Zr}]Zr\text{-DFO-NC318}$ ($\sim 0.8 \mu\text{g}$) + NC318 (0 (control), 20, 100, and 300 μg). Each bar represents the mean ratio \pm SE ($n = 5\text{-}10$ for each group); * $P < 0.05$; ** $P < 0.01$; *** $P < 0.001$ (Student's t -test); indicates a significant difference between the T:B (b) or T:M (c) ratios of each NC318-dosed group compared to respective $[^{89}\text{Zr}]Zr\text{-DFO-NC318}$ controls (0 NC318 μg dose) in Siglec-15+ tissues (lymph nodes, spleen, tumor, and femur). (d, e) $[^{89}\text{Zr}]Zr\text{-DFO-NC318}$ tumor uptakes (%ID/g (d)) and T:M ratios (e) in 624-MEL+S15 ($n = 9$), LOX IMIV ($n = 9$), HCC-827 ($n = 6$), and 624-MEL wild-type (WT; $n = 9$) xenografts after 3 d. Each bar represents the mean (%ID/g or T:M) \pm SE. * $P < 0.05$; ** $P < 0.01$; *** $P < 0.001$ (Student's t -test); indicates a significant difference between the %ID/g (d) or T:M (e) ratios between the indicated 2 tumor types.

T:M; $P = 0.0011$ (vs. 624-MEL+S15); $P = 0.0442$ (vs. LOX IMIV) and 624-MEL WT (7.09 T:M; $P < 0.0001$ (vs. 624-MEL+S15; $P < 0.0021$ (vs. LOX IMIV)) tumor types (Figure 5(e)). These in vivo results indicate that 624-MEL+S15 and LOX IMIV have 2- to 3-fold higher Siglec-15 expression levels compared to HCC-827 and 624-MEL WT which generally agree with the rank order of Siglec-15 expression levels for the same cell lines determined in vitro. However, in vitro, the magnitude of the decreases in Siglec-15 expression levels (B_{max}) was much greater (6- to 12-fold) in LOX IMIV, HCC-827, and 624-MEL WT cells compared to 624-MEL+S15 cells (Figure 2(b)). Most likely these large differences in Siglec-15 expression levels between the tumor cells in vitro and the tumors in vivo are due to the presence of Siglec-15+ immune cells in the tumor microenvironment (TME) which would account for the higher than expected tumor T:Ms with the other tumor types. Further, these results suggest that tumor types with low/negligible Siglec-15 cell surface expression levels such as HCC-827 and 624-MEL WT may possibly be identified in PET imaging studies depending on the contribution from Siglec-15+ immune cells in the TME.

3.4. Small Animal PET Imaging Studies. $[^{89}\text{Zr}]Zr\text{-DFO-NC318}$ (3.7 MBq (100 μCi), associated mass $\sim 20 \mu\text{g}$) was injected into 624-MEL+S15 xenograft mice which were imaged at 1, 3, and 6 d post injection (Figure 6(a)). In the PET images at 1 d post injection, 624-MEL+S15 tumors and spleens were visible but were more easily delineated at 3 d along with lymph nodes due to greater clearance from some nontarget tissues (Figure 6(a)). From PET images obtained at 3 d post injection of $[^{89}\text{Zr}]Zr\text{-DFO-NC318}$ into xenograft mice, 624-MEL+S15 and LOX IMIV tumors were easily visualized with tumor T:Ms of $\sim 20:1$ whereas HCC-

827 and 624-MEL WT had lower tumor T:Ms ranging from 5:1 to 8:1 and not as easily distinguished (Figure 6(b)). These PET imaging results were in agreement with the biodistribution results and further demonstrating that tumors with low to negligible Siglec-15 expression levels may be detectable with $[^{89}\text{Zr}]Zr\text{-DFO-NC318}$ imaging due to the contribution of Siglec-15+ immune cells in the TME.

3.5. Histology and Immunohistochemistry. From the biodistribution studies, 624-MEL+S15, LOX IMIV, HCC-827, and 624-MEL WT tumors were prepared for H&E and IHC staining for Siglec-15, CD31 (vessel density), CD45 (hematopoietic cells including leukocytes, dendritic cells, NK cells, stem cells, and macrophage/monocyte), and Iba1 (macrophages) to confirm Siglec-15 targeting and identify mouse immune cells in the TME (Figure 7(a)). All tumor types were found to have varying degrees of tissue necrosis from H&E staining which were excluded from the quantitative scoring of the Siglec-15 and CD31 IHC results (Figures 7(b) and 7(c)). The LOX IMIV and 624-MEL WT tumor types had the greatest degree of necrosis which may in part be related to the tumor size in which the majority of these tumors ranged from 0.8 to 1.5 g whereas the HCC-827 tumors were smaller < 0.8 g. The vascular density determined from CD31 IHC staining was found to differ among the tumor types with LOX IMIV (49.2 ± 4.5 vessels/ μm^2 ; $n = 6$) exhibiting the highest vessel densities compared to HCC-827 (20.9 ± 1.8 vessels/ μm^2 ; $n = 6$) tumors, 624-MEL+S15 (16.5 ± 1.7 vessels/ μm^2 ; $n = 8$), and 624-MEL WT (13.1 ± 1.4 vessels/ μm^2 ; $n = 6$) which were 2- to 3-fold lower (Figure 7(b)). The highest Siglec-15 expression levels (H -score) were observed in the 624-MEL+S15 (H -score = 93) and LOX IMIV (H -score = 2.6) tumor cells whereas Siglec-15 levels of HCC-827 (H -score = 0.011) and 624-MEL WT

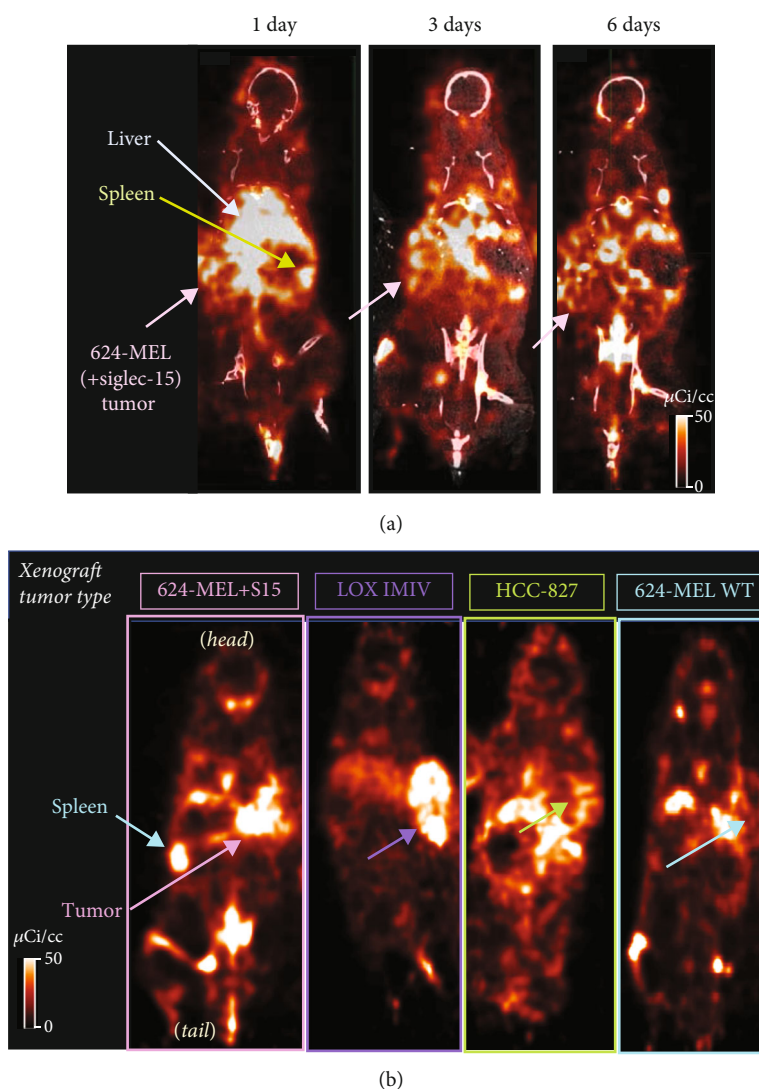


FIGURE 6: (a) Coronal PET/CT images of 624-MEL+S15 mouse xenografts at 1, 3, and 6 d post injection of [^{89}Zr]Zr-DFO-NC318 (3.7 MBq (100 μCi), associated mass~ 20 μg). (b) PET images of 624-MEL+S15, LOX IMIV, HCC-827, and 624-MEL WT mouse xenografts at 3 d post injection of [^{89}Zr]Zr-DFO-NC318 (3.7 MBq (100 μCi), associated mass~ 20 μg).

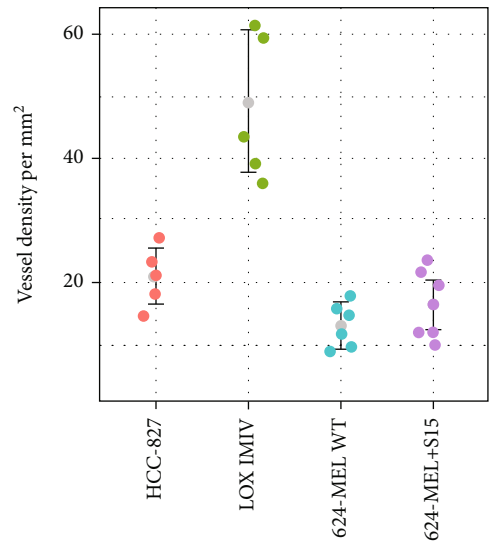
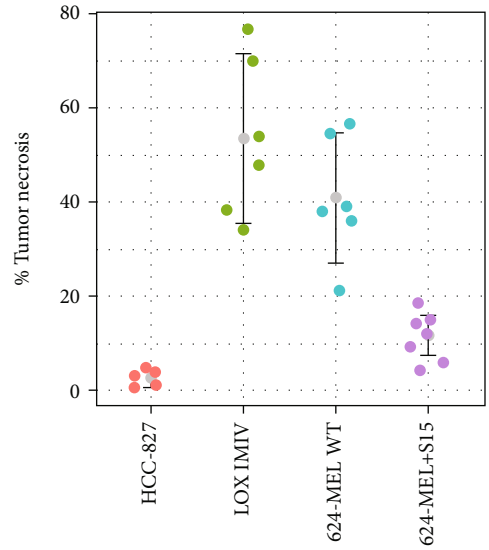
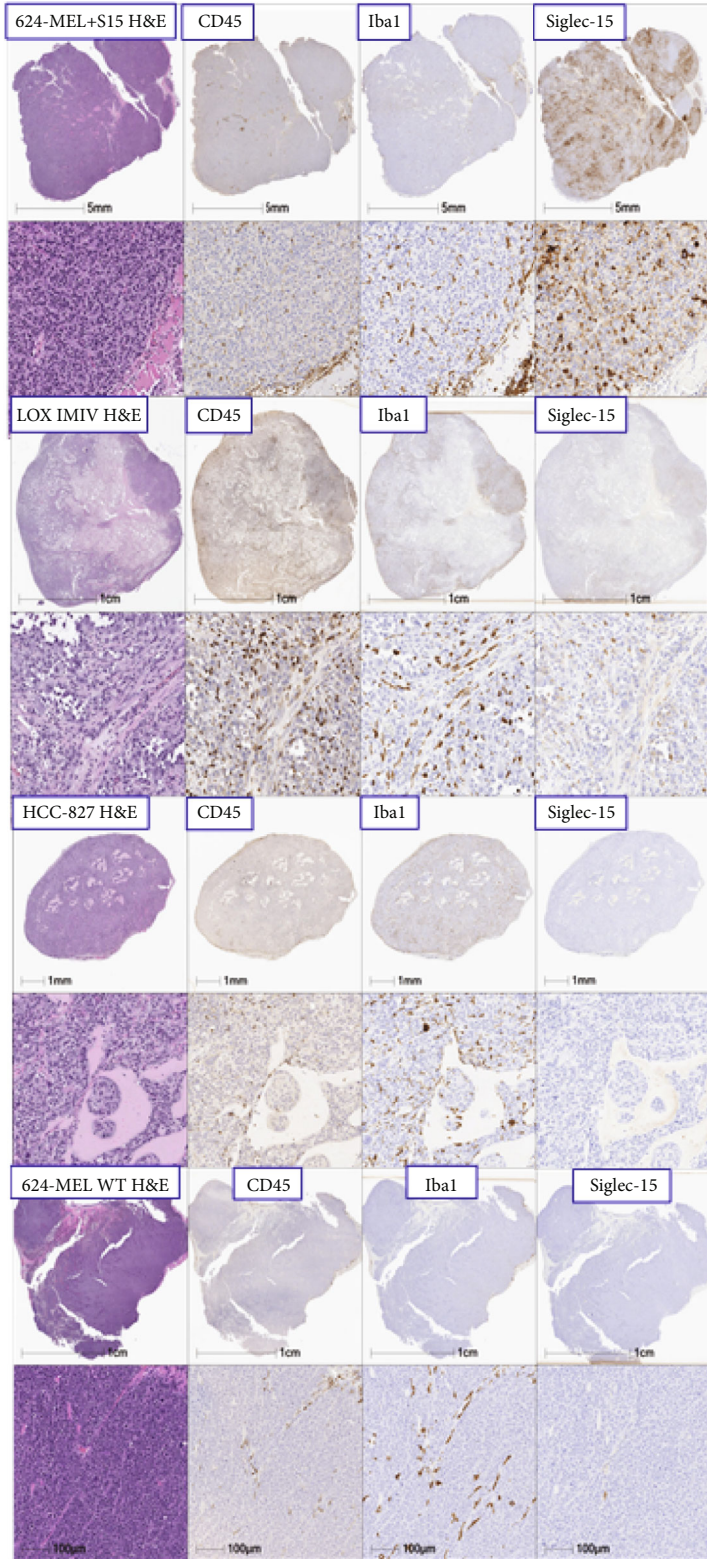
(H -score = 0.23) were hardly above background levels and considered negative for Siglec-15 (Figure 7(c)). The LOX IMIV tumor type (1609 cells per mm^2) exhibited a 3- to 4-fold increase in murine leukocytes (CD-45 IHC) compared to the HCC-827 (552 cells per mm^2), 624-MEL+S15 (395 cells per mm^2), and 624-MEL WT (389 cells per mm^2) tumor types. The LOX IMIV tumor type (665 cells per mm^2) also had the highest number of macrophages (Iba1+) which were comparable to the HCC-827 tumor type (602 cells per mm^2) and 2- to 4-fold higher than the 624-MEL+S15 (293 cells per mm^2) and 624-MEL WT tumor type (158 cells per mm^2 ; Figure 7(c)). Taken together, these results show that immune cell types are present in the TME of the LOX IMIV and HCC-827 tumor types which may express Siglec-15+ and therefore account for a portion of the [^{89}Zr]Zr-DFO-NC318 uptake.

Using dual immunofluorescence staining to distinguish human Siglec-15+ tumor cells from Siglec-15+ murine cells,

624-MEL+S15 was found to have the highest human Siglec-15 expression levels (16.4% NUMA(+)) which was 5- to 6-fold greater than the LOX IMIV (3.1% NUMA(+)) tumor type (Figures 8(a) and 8(b)). These results for the % NUMA(+) cells which represent Siglec-15+ human tumor cells are comparable to the rank order of the Siglec-15 expression levels (B_{max} 's; Figure 2(b)) determined in vitro for each of the tumor cell lines.

In addition to the presence of murine Siglec-15+ positive cells in the TME, murine Siglec-15+ positive cells were generally observed in the spleen and lymph nodes in IHC sections from 624-MEL+S15 xenografts further confirming the specific uptake of [^{89}Zr]Zr-DFO-NC318 in these tissues (Figure 9).

3.6. Dosimetry Estimation for [^{89}Zr]Zr-DFO-NC318. The extrapolation of radioconjugate residence times in humans was determined from the radioactivity content of the organs



(b)

FIGURE 7: Continued.

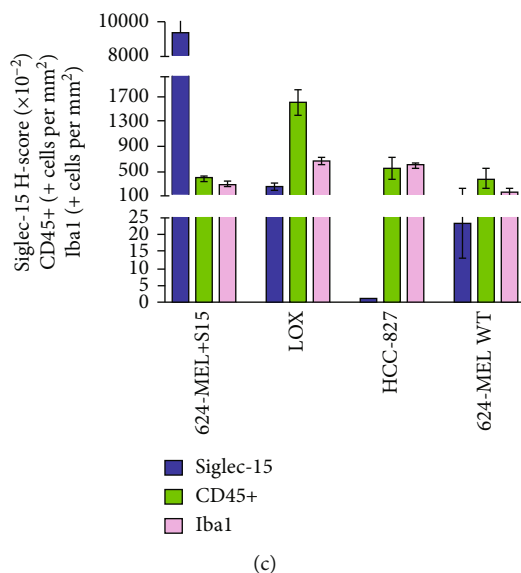


FIGURE 7: (a) Representative images of H&E and IHC stained sections (CD45, Iba1, and Siglec-15) from 624-MEL+S15, LOX IMIV, HCC-827, and 624-MEL WT tumors. (b) Comparison of individual tumor necrosis (%) and vessel density (estimated from CD-31 IHC staining) for the 4 tumor types. (c) IHC quantitative analysis of Siglec-15 expression levels (staining intensity score and H -score) and the number of positive cells per mm^2 for CD45 and Iba1 of the tumor types; each bar represents the mean \pm SE ($n = 8$, 624-MEL+S15 tumors; $n = 6$, LOX IMIV, HCC-827, and 624-MEL WT tumors).

and tissues using the [^{89}Zr]Zr-DFO-NC318 biodistribution results with the Balb/c mice (Table 1). The five highest radiation absorbed doses were observed in the osteogenic cells (1.53 mSv/MBq, 5.67 rem/mCi), red marrow (0.868 mSv/MBq, 3.21 rem/mCi), kidney (0.562 mSv/MBq, 2.08 rem/mCi), adrenals (0.305 mSv/MBq, 1.13 rem/mCi), and spleen (0.278 mSv/MBq, 1.03 rem/mCi). The total body dose was 0.211 mSv/MBq or 0.779 rem/mCi, and the effective dose was 0.250 mSv/MBq or 0.926 rem/mCi.

4. Discussion

[^{89}Zr]Zr-DFO-NC318 demonstrated specific binding to Siglec-15 with nM binding affinity in vitro and discriminated in human cancer cell lines low to moderate concentrations of Siglec-15. In vivo [^{89}Zr]Zr-DFO-NC318 had sufficient stability to be highly retained in Siglec-15+ tumors as well as mouse lymph nodes, spleen, and bone which are known to have murine Siglec-15+ immune cell populations. From these preclinical studies, [^{89}Zr]Zr-DFO-NC318 was found to exhibit appropriate targeting and dosimetry to be considered for clinical applications including patient selection for Siglec-15-targeted immunotherapeutics and then patient monitoring of treatment responses.

Siglec-15 has emerged as a novel immune inhibitor which utilizes a pathway that is distinct from the PD-1/PD-L1 immune checkpoint pathway and therefore may represent the next generation of immunotherapeutics. Preliminary results in mouse tumor models have shown tumor regression in both PD-1 sensitive and insensitive tumors suggesting that Siglec-15-targeted immunotherapeutics may offer an alternative to patients resistant to PD-1/PD-

L1 therapies [22, 23]. In a NC318 clinical trial with NSCLC patients who were refractory for anti-PD-1 mAb therapy, 20% had complete or partial responses and 30% had stable disease [9]. Although the results from this clinical trial are encouraging, the patients were not selected based on their PD-1/PD-L1 or Siglec-15 expression levels, and therefore, more definitive results may be possible with selected populations. Development of diagnostic agents and a predictive biomarker are needed to select patients for Siglec-15-targeted therapeutics and to gain a better understanding of the relationship of the interactions between Siglec-15 positive tumor cells and immune cells in the tumor TME to therapeutic responses. An IHC assay has been developed for patient selection for Siglec-15-targeted therapies which detects Siglec-15+ tumor and immune cells in tumor biopsies [24]. These IHC results reflect the Siglec-15 positivity of the tumor at the time and location of the biopsy and may not reflect changes that have occurred in the TME from the time of the biopsy to the start of therapy or during the therapeutic time course. Since preclinical studies would suggest that the overexpression of Siglec-15 in the TME plays a role in the immunosuppression of the tumor and a therapeutic such as NC318 would act to reverse this immunosuppression in the TME, assessing the dynamic changes in the TME of Siglec-15 expression levels in response to therapy is needed [9]. Immuno-PET imaging with [^{89}Zr]Zr-DFO-NC318 could provide a real-time readout of Siglec-15 expression levels in all lesions of the patient and surrounding tissues as well as monitor changes in expression levels with treatment.

Generally, the uptake of [^{89}Zr]Zr-DFO-NC318 was higher in the lymphoid tissues of the athymic tumor-bearing mice compared to the immunocompetent Balb/c

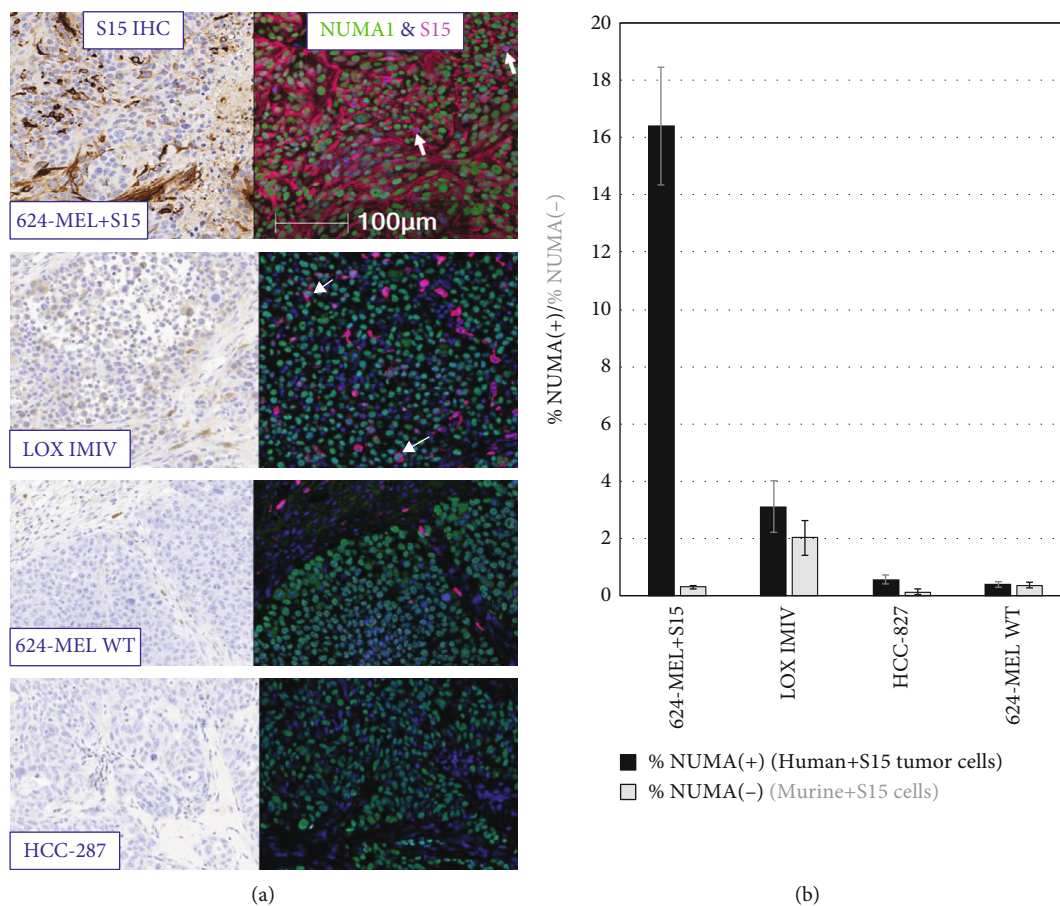


FIGURE 8: (a) Representative images of Siglec-15 (S15) IHC and dual immunofluorescence staining (NUMA1&S15) of 624-MEL+S15, LOX IMIV, HCC-827, and 624-MEL WT tumors from xenograft mice to distinguish positive Siglec-15 (+S15) human tumor cells (green (NUMA1, human nuclear marker) and pink (+S15)) from mouse +S15 immune cells in the TME (blue (mouse) and pink (+S15)); white arrows identify human tumor cells (NUMA(+)) positive for S15. (b) Quantification of human tumor cells positive for S15 (% NUMA(+)) and murine +S15 cells (% NUMA(-)) of each tumor type from dual immunofluorescence stained images; each bar represents the mean \pm SE ($n = 8$, 624-MEL+S15 tumors; $n = 6$, LOX IMIV, HCC-827, or 624-MEL WT tumors).

mice indicating that the athymic mice had increased Siglec-15+ expressing immune cells. Athymic mice are known to have impaired T-cell function with fewer circulating leukocytes and depletion in “thymus dependent” areas of the spleen, lymph nodes, and bone marrow compared to normal mice but have normal cytotoxic responses to T-independent antigens [25, 26]. In contrast, natural killer (NK) cell and macrophage cytotoxic activities have been reported to be enhanced in athymic mice compared to immunocompetent mice suggesting that these immune cell types may compensate for the T-cell deficiency [27]. In particular, athymic mice transplanted with human tumor cells have been found to have allograft cytotoxic responses mediated by macrophages and NK cells [27, 28]. As the tumor progresses, a state of chronic inflammation ensues resulting in the accumulation of myeloid-derived suppressor cells (MDSCs) which is a heterogeneous immature myeloid cell population with immunosuppressive functions that operate by a wide variety of mechanisms [29]. The abnormal production of growth factors and cytokines by the tumor cells and stroma includ-

ing resident macrophages causes expansion of MDSCs by inhibiting normal myeloid differentiation [30]. The expansion of MDSCs has been found to extend beyond the tumor to the spleen of tumor-bearing mice as well as bone marrow cells cultured with tumor cells [31]. Within the cell groups comprising immature MDSCs, a small group phenotypically similar to monocytes (M-MDSCs) can differentiate into macrophages, dendritic cells, and osteoclasts that primarily have immunosuppressive functions both at the tumor site and periphery [31, 32]. Similarly, macrophages induced with growth factors and other innate inflammatory mediators as well as tumor-associated macrophages (TAM) have been found to overexpress Siglec-15 suggesting that a subset of the M-MDSC cells are Siglec-15+ [9]. Taken together the increased cytotoxic activity of macrophages and then the allograft immune response resulting in the expansion of Siglec-15+, M-MDSCs in the spleen, lymph node, and bone marrow of athymic tumor-bearing mice may be expected to account for the increased [^{89}Zr]Zr-DFO-NC318 uptakes observed in these lymphoid tissues.

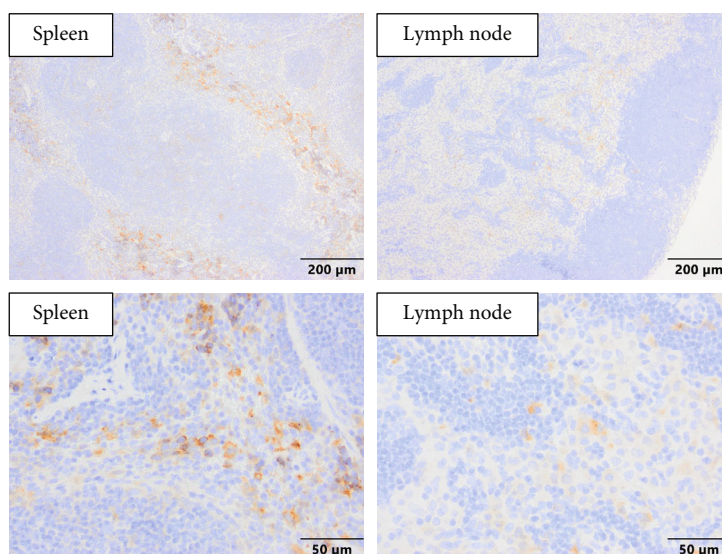


FIGURE 9: Representative Siglec-15 immunohistochemistry stained sections of the spleen and lymph nodes from 624-MEL+S15 xenografts. Spleen: Siglec-15+ cells were commonly observed in the splenic red pulp with a cytoplasmic to membranous staining pattern; lymph node: faint Siglec-15+ cells were commonly observed in the medulla but occasionally were present in the paracortex or cortical regions of the node.

The in vivo [^{89}Zr]Zr-DFO-NC318 uptakes of the 624-MEL+S15, LOX-IMIV, HCC-827, and 624-MEL WT tumors exhibited similar rank order compared to the in vitro (B_{max}) and IHC results; however, the magnitude of the differences in Siglec-15 expression levels between the tumor types in vivo was less than would have been predicted from the in vitro results (B_{max}). Most likely the [^{89}Zr]Zr-DFO-NC318 increased tumor uptakes in LOX IMIV, HCC-827, and 624-MEL WT cell lines can be attributed to the contribution of Siglec-15+ murine immune cells in the TME which was confirmed with IHC. Further LOX IMIV, HCC-827, and 624-MEL WT tumor sections exhibited high levels of CD45+ and Iba1 + immune murine cells indicating the presence of infiltrating immune cells in the TME which in tumor-bearing athymic mice would be expected to include dendritic cells, NK cells, and macrophages. Further, these IHC results indicate that macrophages comprise a majority of the immune cell type in the TME since Iba1 is a marker specific for macrophages whereas the CD45+ marker cells include not only macrophages but T-cells, B-cells, dendritic cells, NK cells, stem cells, and granulocytes [33]. Both macrophages and dendritic cells are known to express Siglec-15; therefore, in the TME, a subset of these immune cell types would be capable of Siglec-15 expression. These preclinical studies would suggest that although tumors have low expression levels of Siglec-15, the presence of Siglec-15+ immune cells in the TME may make possible detection with PET imaging in a clinical setting. However, these preclinical studies are not predictive of the immune cell types nor the Siglec-15+ subset that would comprise the TME in human patients and would require [^{89}Zr]Zr-DFO-NC318 imaging studies in human subjects.

These promising preclinical results would suggest that the [^{89}Zr]Zr-DFO-NC318 would be appropriate for Siglec-15 immuno-PET imaging in human subjects to establish the predictive value of Siglec-15 expression as a reliable biomarker for patient selection in clinical trials, monitoring therapeutic responses and evaluating the efficacy of this new class of immunotherapeutics. Siglec-15 expression in humans is generally absent from normal tissue and confined to myeloid cells and osteoclasts in lymphoid tissues [9, 34]. In normal human spleen and lymph nodes, Siglec-15 expression was found on a small number of dendritic cells and macrophages suggesting that Siglec-15 expression occurs on a subset of dendritic cells or macrophages [35]. In contrast, Siglec-15 expression levels are upregulated in tumors and tumor infiltrating macrophages which may also extend to the spleen, lymph nodes, and other lymphoid tissues. Therefore, in PET images, lesions of cancer patients in which Siglec-15 has been upregulated should be discernible from normal tissue. In addition with whole body PET imaging, changes in Siglec-15 expression levels in the spleen, lymph nodes, and other lymphoid tissues can be assessed to determine the role Siglec-15 plays in cancer progression and M-MDSC biology [31]. Additionally, since NC318 is currently in clinical trials, [^{89}Zr]Zr-DFO-NC318 could be used as a companion diagnostic imaging agent as well as assist in establishing dosing and tracking in vivo the tissue distribution of NC318 to gain a better understanding of off-target side effects. Since NC318 has been found to be safe in on-going clinical trials, clinical translation of [^{89}Zr]Zr-DFO-NC318 can be completed relatively more easily for “proof of concept” PET imaging studies. Providing these studies corroborate the value of Siglec-15 as a predictive biomarker further

TABLE 1: [^{89}Zr]Zr-DFO-NC318 human dosimetry extrapolated from Balb/c mouse biodistributions (includes the organs used in the kinetics input form of OLINDA, the mouse residence times, the extrapolated human residence times, and the dose the tissue received per unit injected activity).

Organ	Mouse residence time (h)	Human residence time (h)	Dose (mSv/MBq)	Dose (rem/mCi)
Adrenals	0.409	0.0170	0.305	1.13
Brain	0.0577	0.0540	0.181	0.669
Breasts	NA	NA	0.0897	0.332
Gallbladder wall	NA	NA	0.153	0.567
LLI wall	NA	NA	0.159	0.588
Small intestine	2.64	0.391	0.154	0.571
Stomach wall	0.189	0.0237	0.119	0.440
ULI wall	NA	NA	0.144	0.534
Heart wall	0.142	0.121	0.150	0.555
Kidneys	0.930	1.24	0.562	2.08
Liver	3.50	1.78	0.253	0.936
Lungs	0.854	1.01	0.218	0.808
Muscle	NA	NA	0.147	0.542
Ovaries	0.0475	0.010	0.135	0.500
Pancreas	0.0885	0.021	0.185	0.685
Red marrow	NA	NA	0.868	3.21
Osteogenic cells	NA	NA	1.53	5.67
Trabecular bone	15.0	40.80	NA	NA
Skin	NA	NA	0.109	0.402
Spleen	0.386	0.256	0.278	1.03
Testes	NA	NA	0.092	0.340
Thymus	0.0845	0.00736	0.136	0.502
Thyroid	0.0321	0.0180	0.202	0.748
Urinary bladder wall	0.0403	0.0298	0.101	0.372
Uterus	NA	NA	0.114	0.423

development of small molecules or Ab fragments targeting Siglec-15 labeled with shorter lived radionuclides (i.e., fluorine-18) would be justified. The faster pharmacokinetics of these imaging agents would allow for same day imaging rather than waiting several days to acquire images which is preferable with whole mAb-based imaging agents.

In conclusion, [^{89}Zr]Zr-DFO-NC318 would make available real-time PET images that represent Siglec-15 tumor expression levels not only for the primary tumor but metastatic lesions as well. In patients with metastatic disease, [^{89}Zr]Zr-DFO-NC318 imaging would make possible the measurement of all Siglec-15+ lesions thereby providing a potentially better tool for patient selection than a biopsy of the primary tumor. Such imaging could also potentially serve as a biomarker to monitor responses in patients undergoing Siglec-15-targeted therapies. Validated PET imaging agents that could identify and quantify tumor Siglec-15 expression levels would be beneficial not only for clinical diagnostic and prognostic applications but also for the drug development process as well.

Data Availability

The data used to support the findings of this study are included within the article and the supplementary information files.

Disclosure

The content of this publication does not necessarily reflect the views or policies of the Department of Health and Human Services nor does mention of trade names, commercial products, or organization imply endorsement by the U.S. Government.

Conflicts of Interest

The authors declare that they have no conflicts of interest.

Acknowledgments

The authors would like to thank Dr. Linda Liu and Dr. Han Myint at NextCure for providing materials (NC318 and 1F7

mAbs) and expertise. This project has been funded in whole or in part with federal funds from the National Cancer Institute, National Institutes of Health, under contract No. 75N91019D00024.

Supplementary Materials

The stability of [^{89}Zr]Zr-DFO-NC318 stored as a saline solution at 4°C was determined using SE-HPLC at 24 h and 48 h following radiosynthesis; a slow decomposition was observed after 48 h (91% intact; Supporting information, Fig. S1; Table S1). In vitro, the stability of [^{89}Zr]Zr-DFO-NC318 in whole human serum at 37°C was determined by SE-HPLC which indicated a 48% decomposition at 4 days (Supporting information, Fig. S2; Table S2) that remained relatively unchanged from 4 d to 7 d. (*Supplementary Materials*)

References

- [1] S. Rashid, D. Song, J. Yuan, B. H. Mullin, and J. Xu, "Molecular structure, expression, and the emerging role of Siglec-15 in skeletal biology and cancer," *Journal of Cellular Physiology*, vol. 237, no. 3, pp. 1711–1719, 2022.
- [2] R. Takamiya, K. Ohtsubo, S. Takamatsu, N. Taniguchi, and T. Angata, "The interaction between Siglec-15 and tumor-associated sialyl-Tn antigen enhances TGF- β secretion from monocytes/macrophages through the DAP12-Syk pathway," *Glycobiology*, vol. 23, no. 2, pp. 178–187, 2013.
- [3] E. J. van Houtum, C. Büll, L. A. Cornelissen, and G. J. Adema, "Siglec signaling in the tumor microenvironment," *Frontiers in Immunology*, vol. 12, article 790317, 2021.
- [4] J. Wang, J. Sun, L. N. Liu et al., "Siglec-15 as an immune suppressor and potential target for normalization cancer immunotherapy," *Nature Medicine*, vol. 25, no. 4, pp. 656–666, 2019.
- [5] F. B. Kang, W. Chen, L. Wang, and Y. Z. Zhang, "The diverse functions of Siglec-15 in bone remodeling and antitumor responses," *Pharmacological Research*, vol. 155, article 104728, 2020.
- [6] J. Munkley, "The role of Sialyl-Tn in cancer," *International Journal of Molecular Sciences*, vol. 17, no. 3, p. 275, 2016.
- [7] L. Chang, Y. J. Chen, C. Y. Fan et al., "Identification of Siglec ligands using a proximity labeling method," *Journal of Proteome Research*, vol. 16, no. 10, pp. 3929–3941, 2017.
- [8] W. Liu, Z. Ji, B. Wu et al., "Siglec-15 promotes the migration of liver cancer cells by repressing lysosomal degradation of CD44," *FEBS Letters*, vol. 595, no. 17, pp. 2290–2302, 2021.
- [9] J. Sun, Q. Lu, M. F. Sanmamed, and J. Wang, "Siglec-15 as an emerging target for next-generation cancer immunotherapy," *Clinical Cancer Research*, vol. 27, no. 3, pp. 680–688, 2021.
- [10] D. Sato, M. Takahata, M. Ota et al., "Siglec-15-targeting therapy protects against glucocorticoid-induced osteoporosis of growing skeleton in juvenile rats," *Bone*, vol. 135, article 115331, 2020.
- [11] D. Sato, M. Takahata, M. Ota et al., "Siglec-15-targeting therapy increases bone mass in rats without impairing skeletal growth," *Bone*, vol. 116, pp. 172–180, 2018.
- [12] M. Stuible, A. Moraitis, A. Fortin et al., "Mechanism and function of monoclonal antibodies targeting Siglec-15 for therapeutic inhibition of osteoclastic bone resorption," *The Journal of Biological Chemistry*, vol. 289, no. 10, pp. 6498–6512, 2014.
- [13] E. M. Jagoda, O. Vaslatiy, F. Basuli et al., "Immuno-PET imaging of the programmed cell death-1 ligand (PD-L1) using a zirconium-89 labeled therapeutic antibody, avelumab," *Molecular Imaging*, vol. 18, 2019.
- [14] C. W. Choi, L. Lang, J. T. Lee et al., "Biodistribution of 18F- and 125I-labeled anti-Tac disulfide-stabilized Fv fragments in nude mice with interleukin 2 alpha receptor-positive tumor xenografts," *Cancer Research*, vol. 55, no. 22, pp. 5323–5329, 1995.
- [15] B. J. Morris, "Specific radioactivity of radioimmunoassay tracer determined by self-displacement: a re-evaluation," *Clinica Chimica Acta*, vol. 73, no. 1, pp. 213–216, 1976.
- [16] S. L. Lindstedt and P. J. Schaeffer, "Use of allometry in predicting anatomical and physiological parameters of mammals," *Laboratory Animals*, vol. 36, no. 1, pp. 1–19, 2002.
- [17] M. A. Keenan, M. G. Stabin, W. P. Segars, and M. J. Fernald, "RADAR realistic animal model series for dose assessment," *Journal of Nuclear Medicine*, vol. 51, no. 3, pp. 471–476, 2010.
- [18] F. Kuo, S. Histed, B. Xu et al., "Immuno-PET imaging of tumor endothelial marker 8 (TEM8)," *Molecular Pharmaceutics*, vol. 11, no. 11, pp. 3996–4006, 2014.
- [19] G. Murugesan, V. G. Correia, A. S. Palma et al., "Siglec-15 recognition of sialoglycans on tumor cell lines can occur independently of sialyl Tn antigen expression," *Glycobiology*, vol. 31, no. 1, pp. 44–54, 2021.
- [20] D. S. Abou, T. Ku, and P. M. Smith-Jones, "In vivo biodistribution and accumulation of ^{89}Zr in mice," *Nuclear Medicine and Biology*, vol. 38, no. 5, pp. 675–681, 2011.
- [21] A. Moroz, C. Y. Lee, Y. H. Wang et al., "A preclinical assessment of (^{89}Zr) Zr-atezolizumab identifies a requirement for carrier added formulations not observed with (^{89}Zr) Zr-C4," *Bioconjugate Chemistry*, vol. 29, no. 10, pp. 3476–3482, 2018.
- [22] O. De Henau, M. Rausch, D. Winkler et al., "Overcoming resistance to checkpoint blockade therapy by targeting PI3K γ in myeloid cells," *Nature*, vol. 539, no. 7629, pp. 443–447, 2016.
- [23] D. A. Reardon, P. C. Gokhale, S. R. Klein et al., "Glioblastoma eradication following immune checkpoint blockade in an orthotopic, immunocompetent model," *Cancer immunology research*, vol. 4, no. 2, pp. 124–135, 2016.
- [24] S. Shafi, T. N. Aung, C. Robbins et al., "Development of an immunohistochemical assay for Siglec-15," *Laboratory Investigation*, vol. 102, no. 7, pp. 771–778, 2022.
- [25] M. Pelleitier and S. Montplaisir, "The nude mouse: a model of deficient T-cell function," *Methods and Achievements in Experimental Pathology*, vol. 7, pp. 149–166, 1975.
- [26] R. Romano, L. Palamaro, A. Fusco et al., "From murine to human nude/SCID: the thymus, T-cell development and the missing link," *Clinical & Developmental Immunology*, vol. 2012, article 467101, pp. 1–12, 2012.
- [27] W. Budzynski and C. Radzikowski, "Cytotoxic Cs in immunodeficient athymic mice," *Immunopharmacology and Immunotoxicology*, vol. 16, no. 3, pp. 319–346, 1994.
- [28] R. Yoshida, "MHC class I recognition by monocyte/macrophage-specific receptors," *Advances in Immunology*, vol. 124, pp. 207–247, 2014.
- [29] C. Groth, X. Hu, R. Weber et al., "Immunosuppression mediated by myeloid-derived suppressor cells (MDSCs) during tumour progression," *British Journal of Cancer*, vol. 120, no. 1, pp. 16–25, 2019.

- [30] N. Kamran, M. Chandran, P. R. Lowenstein, and M. G. Castro, "Immature myeloid cells in the tumor microenvironment: implications for immunotherapy," *Clinical Immunology*, vol. 189, pp. 34–42, 2018.
- [31] D. Marvel and D. I. Gabrilovich, "Myeloid-derived suppressor cells in the tumor microenvironment: expect the unexpected," *The Journal of Clinical Investigation*, vol. 125, no. 9, pp. 3356–3364, 2015.
- [32] N. Kumari and S. H. Choi, "Tumor-associated macrophages in cancer: recent advancements in cancer nanoimmunotherapies," *Journal of Experimental & Clinical Cancer Research*, vol. 41, no. 1, p. 68, 2022.
- [33] G. Liu, H. Ma, L. Jiang, and Y. Zhao, "Allograft inflammatory factor-1 and its immune regulation," *Autoimmunity*, vol. 40, no. 2, pp. 95–102, 2007.
- [34] D. Mansorunov, N. Apanovich, P. Apanovich et al., "Expression of immune checkpoints in malignant tumors: therapy targets and biomarkers for the gastric cancer prognosis," *Diagnostics*, vol. 11, no. 12, p. 2370, 2021.
- [35] T. Angata, Y. Tabuchi, K. Nakamura, and M. Nakamura, "Siglec-15: an immune system Siglec conserved throughout vertebrate evolution," *Glycobiology*, vol. 17, no. 8, pp. 838–846, 2007.